# Nanoscale

## PAPER

# Assisted deposition of nano-hydroxyapatite onto exfoliated carbon nanotube oxide scaffolds

H. Zanin,[a,b] C. M. R. Rosa,[a] N. Eliaz,[c] P. W. May,[d] F. R. Marciano[a] and A. O. Lobo*[a]

Electrodeposited nano-hydroxyapatite (nHAp) is more similar to biological apatite in terms of microstructure and dimension than apatites prepared by other processes. Reinforcement with carbon nanotubes (CNTs) enhances its mechanical properties and increases adhesion of osteoblasts. Here, we carefully studied nHAp deposited onto vertically aligned multi-walled CNT (VAMWCNT) scaffolds by electrodeposition and soaking in a simulated body fluid (SBF). VAMWCNTs are porous biocompatible scaffolds with nanometric porosity and exceptional mechanical and chemical properties. The VAMWCNT films were prepared on a Ti substrate by a microwave plasma chemical vapour deposition method, and then oxidized and exfoliated by oxygen plasma etching (OPE) to produce graphene oxide (GO) at the VAMWCNT tips. The attachment of oxygen functional groups was found to be crucial for nHAp nucleation during electrodeposition. A thin layer of plate-like and needle-like nHAp with high crystallinity was formed without any need for thermal treatment. This composite (henceforth referred to as nHAp–VAMWCNT–GO) served as the scaffold for in vitro biomineralization when soaked in the SBF, resulting in the formation of both carbonate-rich and carbonate-poor globular-like nHAp. Different steps in the deposition of biological apatite onto VAMWCNT–GO and during the short-term biomineralization process were analysed. Due to their unique structure and properties, such nano-bio-composites may become useful in accelerating in vivo bone regeneration processes.

## 1. Introduction

Electrodeposited nano-hydroxyapatite (nHAp) is similar to the mineral component of natural bone in terms of microstructure and dimension, and shows excellent biocompatibility, bioactivity and osteo-conductivity.[1–3] Due to these properties, nHAp has long been evaluated for bone tissue reconstruction.[4] However, its poor mechanical properties (e.g. low fracture toughness and tensile strength) have limited its use in load-bearing applications and/or large bone defects.[5]

Several approaches have been examined to impart mechanical integrity to the nHAp without diminishing its bioactivity.[5] Various forms of carbon seem attractive candidates in this regard,[1,6] with their unprecedented mechanical properties (high strength and toughness) and physicochemical properties (high surface area, electrical and thermal conductivity, and low mass). In particular, carbon nanotubes (CNTs) and graphene have recently gained much attention.[7] Lahiri et al. quantified the adhesion of osteoblasts (cells that synthesise bone) to HAp/MWCNTs using a nano-scratch technique.[8] CNTs were found to increase the adhesion strength, spreading and attachment of osteoblasts. The latter was related to their affinity to conjugate with integrin and other proteins. Balani et al.[9] reported osteoblast growth and proliferation during cell culture on a HAp/CNT composite prepared by plasma spraying. Successful growth of the cells was taken as evidence that the composite was non-toxic. In addition, the CNT significantly improved both the fracture toughness and increased the crystallinity of the coating.

Rath et al.[10] demonstrated improvement of the mechanical properties of electrophoretically deposited HAp–chitosan composite with 10–15 wt% MWCNT. Im et al.[11] also reported improvement in the mechanical properties of chitosan–HAp by incorporating single-walled CNTs (SWCNTs). More recently, Kim et al.[12] presented a spark plasma sintering method to prepare HAp reinforced with the CNT. It was shown that the addition of the CNT to HAp increased the hardness and fracture toughness by 3 to 4 times, indicating that the CNTs are good candidates as reinforcements for strengthening the ceramic matrix.

[a]Laboratory of Biomedical Nanotechnology/Institute of Research and Development (IP&D) at the University of Vale do Paraiba (UniVap), Av. Shishima Hifumi, 2911, Sao Jose dos Campos, 12244-000 SP, Brazil. E-mail: aolobo@pq.cnpq.br, lobo.aol@gmail.com; Fax: +55123947-6717; Tel: +55123947-1100
[b]Laboratory of Energy Storage & Supply (ES&S), IP&D/Univap, Sao Jose dos Campos, São Paulo, Brazil
[c]Department of Materials Science and Engineering, Tel-Aviv University, Ramat Aviv, Tel Aviv 6997801, Israel
[d]School of Chemistry, University of Bristol, Bristol BS8 1TS, UK

Previously, our group[13,14] has presented electrodeposition as an effective, fast and low-cost technique to prepare nHAp layers onto modified vertically aligned multi-walled carbon nanotubes (VAMWCNTs). VAMWCNTs are very interesting biocompatible scaffolds with nanometric porosity and exceptional mechanical and chemical properties. However, the majority of as-grown CNTs are superhydrophobic, which limits their application in aqueous media. To improve wettability, the CNT was functionalized by attaching carboxylic and other oxygen polar groups using oxygen plasma treatment. These functional groups on the CNT surface were found to be crucial for nHAp nucleation during electrodeposition. By adjusting the pH, temperature and current density, the crystal orientation could be controlled. A mechanism for the growth of plate-like nHAp on the functionalized CNT was proposed, suggesting that the carboxylic acid/carboxylate functional groups directly attached to the CNT were essential for accelerated hydroxyl ion release and subsequent deposition of plate-like nHAp crystals. However, to-date, no correlation has been shown between the nHAp crystals synthesized at pH ~6 and the biological apatite that forms during short periods of soaking in the simulated body fluid (SBF).

Kawashita and co-workers[15] suggested that the carboxylate groups facilitate the initial deposition of calcium ions, and that the attraction of calcium ions is an important initial step in calcium phosphate formation. Lee et al.[16] found that the formation of a poly(dopamine) (PDA) ad-layer on the CNT surface made it bioactive. This approach enabled efficient interaction between the CNT and mineral ions (e.g. $Ca^{2+}$), which facilitated the mineralization of HAp. PDA-functionalised CNTs highly accelerated the formation of nHAp when incubated in a SBF, and exhibited a minimal cytotoxic effect on bone osteoblast cells compared to pristine or carboxylated CNTs.

Soaking in SBF is one commonly used approach to induce apatitic calcium phosphate formation on different substrates. The standard SBF (1×) has relatively low calcium ion and phosphate ion concentrations, requiring up to 1 week for the nucleation to begin.[17] The nucleation and precipitation of calcium phosphate from SBFs are faster when a concentrated SBF (e.g. 1.5×) is used.[18]

While the reinforcement effect of CNTs on HAp[8–12,16] and the low cytotoxicity of the composite material[8] have been demonstrated, very little has been reported on the step-by-step formation of HAp on MWCNTs. In this work we used exfoliated VAMWCNTs which have been surface oxidised (VAMWCNT–GO) as an inducing template for nHAp electrodeposition at pH ~6, forming a nHAp–VAMWCNT–GO composite. Furthermore, we soaked this composite in a concentrated SBF at pH ~7.4 and studied the biomineralization process from its early stage until a dense biological apatite layer was formed.

# 2.  Materials and methods

### 2.1.  Preparation of VAMWCNT–GO scaffolds

VAMWCNT scaffolds were prepared using a microwave plasma chemical vapour deposition (CVD) chamber operating at 2.45 GHz. More information on this process is provided elsewhere.[19] The substrates were commercially pure Ti sheets (10 mm × 10 mm × 0.5 mm) covered with a 10 nm-thick Ni layer deposited by electron-beam evaporation. The Ni layer was heated from 350 to 800 °C over a period of 5 min in a $N_2/H_2$ (10/90 sccm) plasma, inducing the formation of nanoparticles which promote the CNT growth. VAMWCNT growth was initiated by introducing $CH_4$ (14 sccm) into the chamber for 1 min, maintaining a substrate temperature of 800 °C and a reactor pressure of 30 Torr. After growth, the sample was introduced into a plasma enhanced CVD reactor (−700 V, pulse frequency 20 kHz) with an oxygen flow rate of 1 sccm at a pressure of 150 mTorr for 2 min.[20] This procedure is known as oxygen plasma etching (OPE), and it is performed in order to exfoliate the CNTs and to improve their wettability by attaching oxygen functional groups on the VAMWCNT surface.[21]

### 2.2.  Electrodeposition of nHAp

We electrodeposited nHAp crystals on VAMWCNT–GO scaffolds using a standard three-electrode cell controlled by an Autolab PGSTAT 128N potentiostat–galvanostat. The VAMWCNT–GO scaffold was employed as a working electrode by inserting it inside a copper/Teflon electrochemical cell, which exposed a fixed electrode area (~0.27 cm$^2$) to the solution, and also established an electrical contact to a copper rod on the back-side (see Fig. 1). A platinum mesh was used as the counter electrode, while Ag/AgCl (3 M KCl (aq.)) was used as the reference electrode. The electrolyte solution used was 0.042 mol l$^{-1}$ of $Ca(NO_3)_2 \cdot 4H_2O$ + 0.025 mol l$^{-1}$ of $(NH_4)_2HPO_4$. All chemicals (Sigma Aldrich) were of high chemical grade. The pH was adjusted to 5.8 and automatically measured throughout the process of electrodeposition using a pX1000 real time pH meter (Metrohm). A magnetic stirrer and a thermostatic bath were used to maintain the process at constant agitation and temperature (~70 °C), respectively. The nHAp crystals were produced on the VAMWCNT–GO electrodes by applying a constant potential of −2.0 V[13] for 20 min. This set-up was chosen to promote stoichiometric nHAp with a Ca/P ratio of ~1.67. We shall henceforth refer to this sample as a nHAp–VAMWCNT–GO composite.
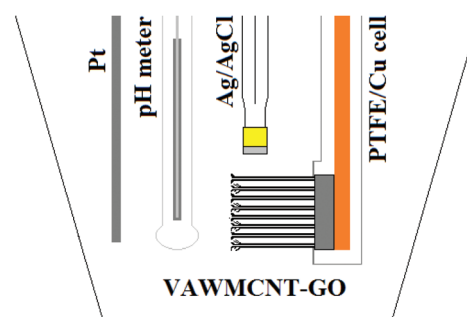


**Fig. 1** Schematic representation of the experimental set-up. The VAMWCNT–GO is drawn enlarged and is not to scale.

**Table 1** Composition of the SBF 1.5×

| Compound | Concentration (mM) |
| --- | --- |
| NaCl | 92.877 |
| KCl | 2.598 |
| $K_2HPO_4$ | 2.027 |
| $CaCl_2 \cdot 2H_2O$ | 4.270 |
| $MgCl_2 \cdot 6H_2O$ | 3.543 |
| $NaHCO_3$ | 4.099 |
| $Na_2SO_4$ | 0.825 |

### 2.3. Bioactivity assay

The SBF (1.5×) solution[18] was prepared by dissolving the compounds listed in Table 1 in distilled water. The pH of the solutions was adjusted with a pH meter (Metrohm) to 7.4 by adding NaOH drops, thus bringing it to the value of blood plasma.

The nHAp–VAMWCNT–GO composites were immersed in polyethylene containers with 15 ml of the SBF, placed in a refrigerated benchtop incubator (Cientec CT-713), and centrifuged at 75 rpm at a temperature of 36.5 °C for different periods of time, from 30 min to 7 days, with the pH being continuously monitored as before.

### 2.4. Analytical characterization

The as-grown VAMWCNT, VAMWCNT–GO, and nHAp–VAMWCNT–GO samples were characterized by several analytical techniques, before and after biomineralization.

Surface area measurements were carried out using a Quanta Chrome Nova Win model 1000 for multi-point Brunauer–Emmett–Teller (BET) adsorption using the classical helium-void volume method. The surface morphology was characterized by high-resolution scanning electron microscopy (HRSEM, FEI Inspect F50, JEOL 6330, and Zeiss EVO Ma10) operated at 20–30 kV. No conductive coating was applied for better SEM imaging. Structural analyses of as-grown VAMWCNT and VAMWCNT–GO were performed using high-resolution transmission electron microscopy (HRTEM, JEOL 3010 operated at 300 kV with a $LaB_6$ filament). A Renishaw laser Raman spectrometer excited by an argon-ion laser ($\lambda$ = 514.5 nm) and operated at room temperature was used for structural analyses of as-grown VAMWCNT and VAMWCNT–GO. The spot size was 15 μm and the laser power was ~6 mW. X-ray photoelectron spectroscopy (VSW H100 spectrometer, $<10^{-10}$ Torr base pressure) was used to identify the oxygen-containing groups on the as-grown VAMWCNT and VAMWCNT–GO surfaces. The semi-quantitative analysis of chemical elements was done by energy-dispersive X-ray spectroscopy (EDS) measurements using an Inca Penta FET x3 system (Oxford Instruments). The estimation of the Ca/P ratio was performed considering Ca (at%) + P (at%) = 100 at%.

A Krüss Easy-Drop system employing the sessile-drop method was used to evaluate the wettability of samples by measuring the contact angle (CA) of the as-grown VAMWCNT and VAMWCNT–GO samples. High-purity deionised water

drops were used for this purpose. Semi-quantitative elemental analyses of calcium and phosphorus contents in the nHAp–VAMWCNT and nHAp–VAMWCNT–GO composites, before and after biomineralization, were carried out with a micro energy dispersive X-ray spectrometer (μ-EDX 1300, Shimadzu, Kyoto, Japan), equipped with a rhodium X-ray tube and a Si (Li) detector cooled using liquid nitrogen. Surface chemical compositions of the two composites, before and after biomineralization, were studied by Fourier transform infrared attenuated total reflection spectroscopy (ATR-FTIR, Perkin-Elmer Spectrum Spotlight-400). Structural analysis of the composites, before and after biomineralization, was performed by X-ray diffraction (XRD, Philips X-Pert) with Cu-Kα radiation generated at 40 kV and 50 mA. The crystallite size of the nHAp phase was calculated based on the peak broadening of the XRD reflection using the Scherrer equation.[13] All XRD patterns were compared to the carbonated HAp (CHAp) powder sample standard (JCPDS 00-004-0697). Measurements were performed in triplicate.

## 3. Results and discussion

### 3.1. Exfoliation of carbon nanotubes

Micrographs of the aligned carbon nanotube films are presented in Fig. 2(a–l). A side view SEM micrograph of the as-grown VAMWCNTs is shown in Fig. 2(a), revealing a highly dense forest of tubes, high porosity, and a film thickness of around 40 μm with a carpet-like structure when viewed from above. Fig. 2(e, i) are top view SEM micrographs of carpet-like CNTs showing different areas which expose (e) tips and (i) tube walls after OPE. Fig. 2(b–d, f, g, j) show higher resolution SEM micrographs from the OPE-treated material, revealing defects caused by exfoliation and oxidation of CNT tips and walls. This effect is more pronounced at the tips because they are more exposed to the plasma, which causes etch pits. However, Fig. 2(i, j) demonstrate details of the exfoliation of the CNT walls, which are more crystalline zones of this material. From this result we conclude that, although amorphous or defective $sp^2$ carbon is expected to be more suitable for exfoliation, the latter occurs also at highly crystalline CNT walls to which the OPE has access. TEM micrographs, Fig. 2(h, k, l), show the CNTs before (h) and after (k, l) OPE. Based on these micrographs, the interplanar spacing of graphite is ~0.34 nm, which is not altered by oxygen plasma treatment.

By comparing TEM micrographs before and after OPE, defects are evidently caused by OPE at the CNT tips and walls. From these observations we can begin to understand the CNT exfoliation process. CNTs are hollow tubular structures with the walls formed by one-atom-thick sheets of carbon, called graphene.[22] Since CNTs are composed of rolled up graphene sheets, once exfoliated, the ends of these graphene sheets become exposed.[23] This OPE process is always concomitant with the attachment of oxygen functional groups on the carbon surface. But, depending on the plasma conditions it was possible to etch the whole or only part of the nanotubes,
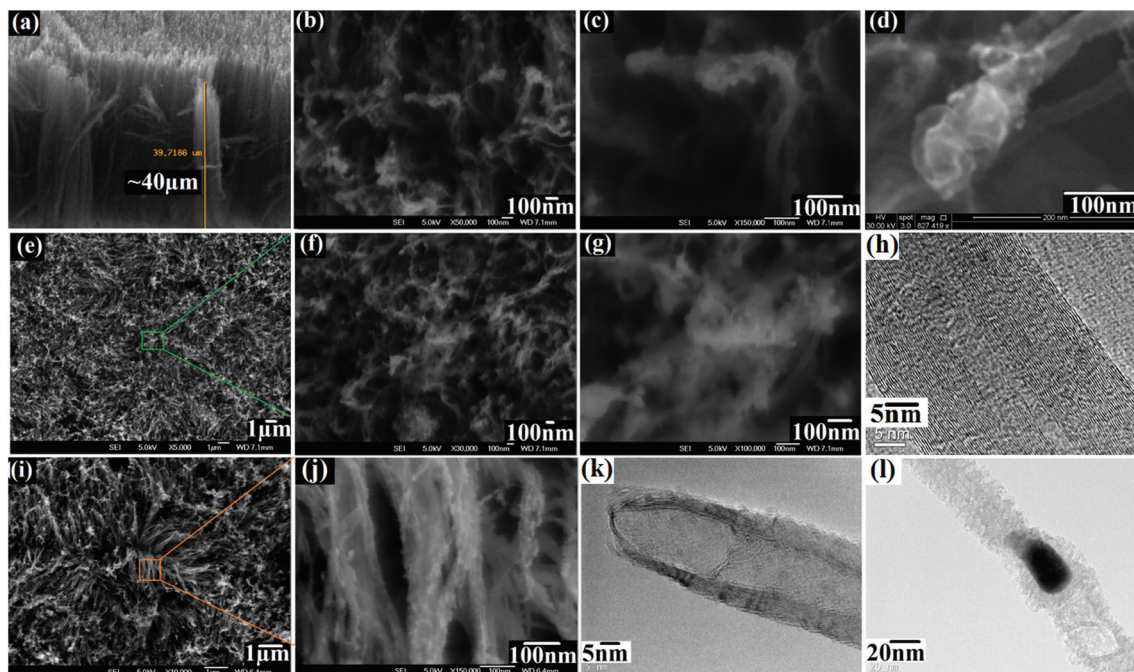
**Fig. 2** SEM (a–g, i, j) and TEM (h, k, l) micrographs of VAMWCNT forest films: (a) as-grown, and (b–l) after oxygen plasma etching.

or simply attach oxygen groups to them without exfoliation (see Fig. 2 in ref. 20). At higher plasma pressures (80–180 mTorr), or for longer process times, erosion was complete. With a diffuse plasma or too low pressure, exfoliation did not occur, but wettability increased significantly because of the attachment of oxygen groups. The VAMWCNT–GO composites were achieved using quite specific conditions. The measured BET surface area of the VAMWCNT was around 930 $m^2$ $g^{-1}$, which seems to be consistent with our estimation using image analysis of selected micrographs of the highly dense forest of tubes. This estimation is based on a calculation of the outer surface area per unit of mass ($S_m$) of the aligned MWCNT, considering its density, diameter and length. To this end, we employed ImageJ software to estimate the number of tubes per unit of area ($N$) $\sim 2.7 \times 10^{15}$ tubes per $m^2$. This value, multiplied by the area of each tube ($A_t = 2 \times \pi \times r \times L$) $\sim 2.51 \times 10^{-12}$ $m^2$ and divided by the total mass ($m$) [bulk density (0.21 g $cm^{-3}$) × volume (40 $cm^3$)] $\sim 8.4$ g, gives a value for $S_m = (N \times A_t)/m \sim 810$ $m^2$ $g^{-1}$.

The OPE causes structural modification in the VAMWCNT sample, as evidenced from its Raman spectra. Fig. 3(a, b) show first- and second-order Raman spectra of VAMWCNT films before and after OPE, respectively. Deconvolutions were performed using a Lorentzian function for the D and G bands, and a Gaussian function for the bands around 1250, 1480–1520 and 1622 $cm^{-1}$ (D′ shoulder).[24] The D band is usually attributed to the disorder and imperfection of the carbon crystallites.[25] The G band is assigned to one of the two $E_{2g}$ modes corresponding to stretching vibrations in the basal plane ($sp^2$ domains) of single-crystal graphene.[26] In the first-order spectra, for appropriate fitting, two Gaussian peaks

centred at around 1250 and 1480 $cm^{-1}$ were added. The origin of the shoulder is most likely a double resonance process, because its Raman shift ($\sim 1200$ $cm^{-1}$) is a point on phonon dispersion curves. These results are reproducible and in complete agreement with our past results.[27]

Fig. 3(c, d) show C 1s fitted XPS spectra recorded from VAMWCNT and VAMWCNT–GO samples before (c) and after (d) OPE. The C 1s curves were deconvoluted into six peaks, at around 284.1, 285.4, 287.1, 288.7, 290.1 and 291.6 eV.[28] The peaks correspond to aliphatic carbons ($sp^2$ hybridization), defects, carbon atoms with C–O, –C═O, carbonates and shake-up peaks ($\pi$–$\pi^*$ transitions), respectively.[20] From the C 1s curves we observed the increase of both oxygen-group content and defects, in agreement with the Raman spectra. This infers the formation of strong C–O bonds from the oxygen-containing groups that are situated along the CNT.[29] The OPE creates open-ended termini in the structure, which are stabilized by –COOH and –OH groups, which remain bonded to the nanotubes at the end termini and/or the sidewall defect sites. OPE increased the oxygen content from $\sim 5\%$ (Fig. 3(c)) to $\sim 20\%$ (Fig. 3(d)) after OPE treatment, which was estimated by the procedure described by Payne et al.[30] From the previous analysis and from the XPS spectra we can conclude that the OPE attaches oxygen-containing groups on the CNT that improve its wettability and negatively charge its surface (see also Fig. 4a in ref. 31). Concerning the surface energy of VAMWCNT and VAMWCNT–GO samples, the as-grown samples exhibited superhydrophobic behaviour while the OPE-treated samples exhibited a superhydrophilic surface. This conclusion is based on the measurement of the contact angle (CA) between water drops and the sample surface, as shown in the inset in Fig. 3(c, d).
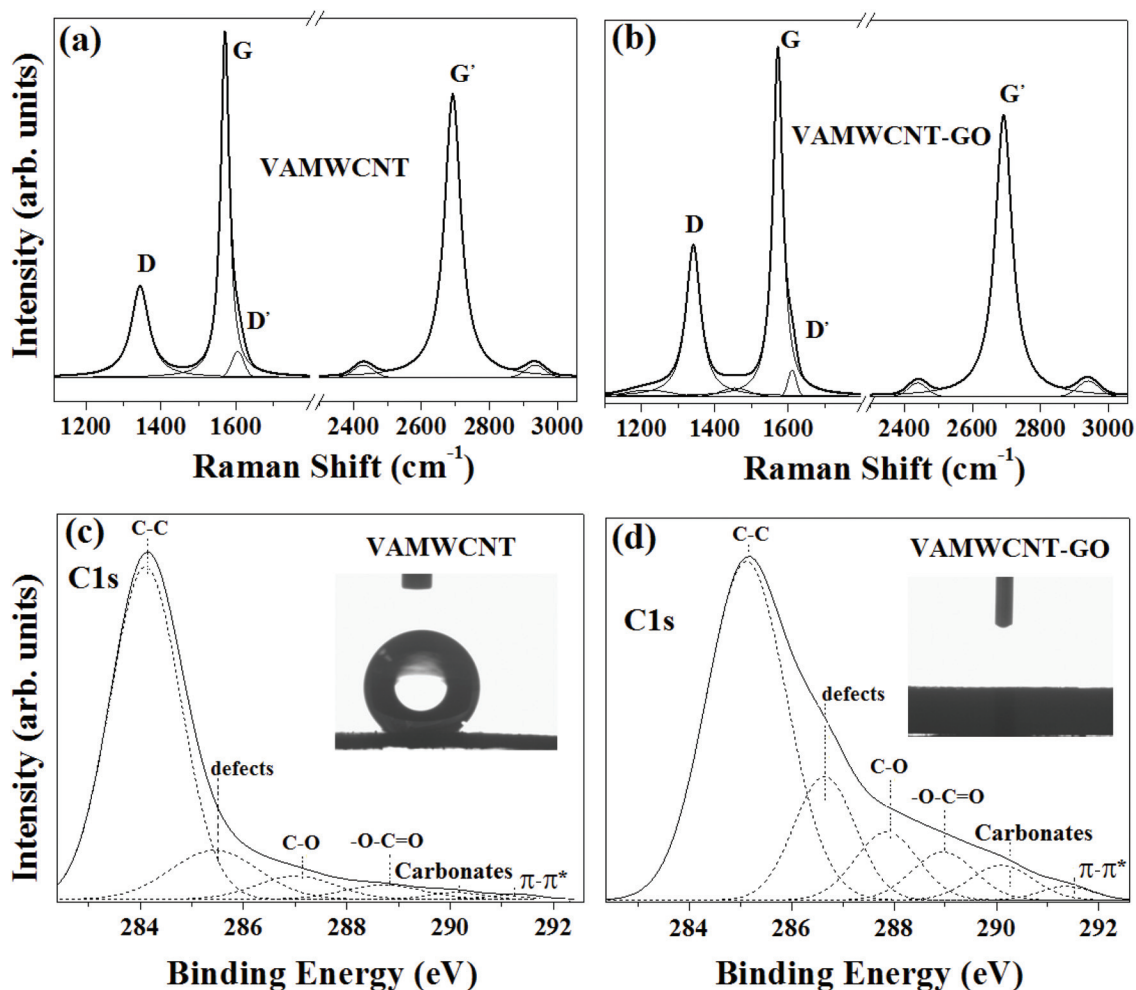
**Fig. 3** (a, b) First- and second-order Raman spectra, (c, d) XPS C 1s energy spectra: (a, c) as-grown VAMWCNT, (b, d) VAMWCNT–GO, with their deconvoluted peak fits. Insets in (c, d) are images of the contact angle measurements for water drops on the superhydrophobic (c) and superhydrophilic (d) surfaces.

The superhydrophobic surface is associated with a CA ~ 157°, whereas the superhydrophilic surface shows a CA ~0°.

The carboxylic acid groups detected by XPS analysis improved the wettability and also attracted $Ca^{2+}$ ions from the aqueous media to the surface, which is very important for HAp formation. The carboxylate group binds to $Ca^{2+}$, forming sites that attract $PO_4^{3-}$ anions, thus eventually forming a continuous calcium phosphate coating during electrodeposition.

### 3.2. Electrodeposition of plate- and needle-like nHAp onto VAMWCNT–GO

Fig. 4(a–c) show the electrochemical response of VAMWCNT–GO, VAMWCNT and Ti electrodes in 0.042 mol $l^{-1}$ Ca$(NO_3)_2 \cdot 4H_2O$ + 0.025 mol $l^{-1}$ $(NH_4)_2HPO_4$. Fig. 4(a) compares cyclic voltammograms (CVs) from VAMWCNT–GO with those from VAMWCNT and Ti electrodes at pH = 5.8. From these CVs we can conclude that the oxidised surface at the CNT tips creates electroactive sites enhancing charge transfer across the CNT/electrolyte interface.[32] As a direct result, VAMWCNT–GO

has both a higher current capacitance and current density than VAMCNTs or Ti electrodes. Considering VAMWCNTs before and after OPE, it is clear that OPE enhances the current stability of VAMWCNT electrodes (Fig. 4(b)) during the potentiostatic electrodeposition of nHAp at −2.0 V vs. Ag/AgCl. Fig. 4(c) shows a pH decrease to more acidic levels due to an oxidation reaction taking place at the anode (2 $H_2O(l) \rightarrow O_2(g) + 4H^+(aq.) + 4e^-$), which forms $H^+$ during water splitting.

The pH was measured between the working electrode and the counter electrode, as illustrated in Fig. 1. The shape of the current transient is different, and the measured current density is much higher than those reported by Eliaz and Sridhar[33] for the electrodeposition of HAp on CP-Ti at either pH = 4.2 or pH = 6.0. However, the applied potential in ref. 33 was −1.4 V vs. SCE (i.e. −1.356 V vs. Ag/AgCl), which resulted in less hydrogen evolution. The extensive hydrogen evolution in the present work may be responsible for the noisy and unsteady current transient. While the kinetics of nucleation is promoted by the high overpotential, crystal growth is sup-
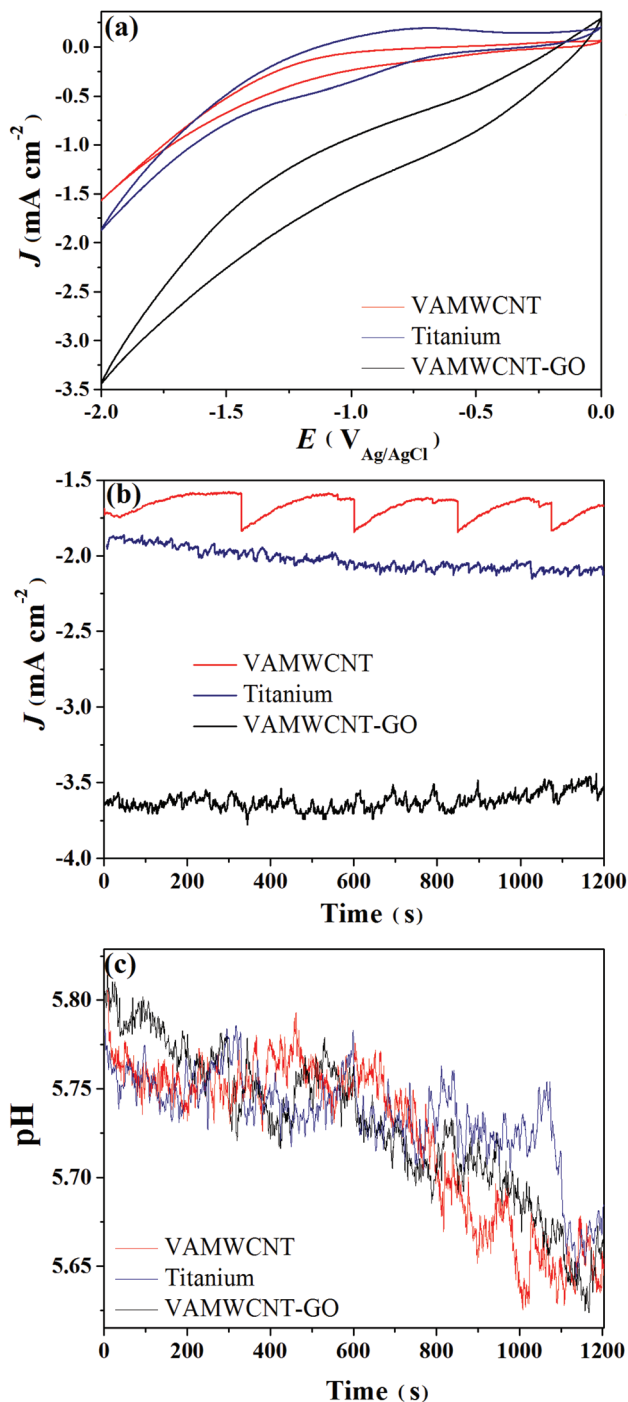
Fig. 4 (a) Cyclic voltammograms of VAMWCNT–GO, VAMWCNT and titanium electrodes taken at 100 mV s$^{-1}$ in 42 mM Ca (NO$_3$)$_2$·4H$_2$O + 25 mM (NH$_4$)$_2$HPO$_4$. Current density (b) and pH (c) transients during electrodeposition of nHAp on electrodes at −2 V vs. Ag/AgCl and T = 70 °C.



Fig. 5 SEM (a, b) and HRTEM (c) micrographs of plate- and needle-like nHAp electrodeposited on VAMWCNT–GO composites for 20 min.

pressed by the intensive H$_2$ evolution. As a consequence, smaller nHAp crystals are formed and the coating is governed by secondary nucleation processes.

Fig. 5(a–c) show SEM and HRTEM micrographs of nHAp electrodeposited onto VAMWCNT–GO for 20 min. Fig. 5(a)
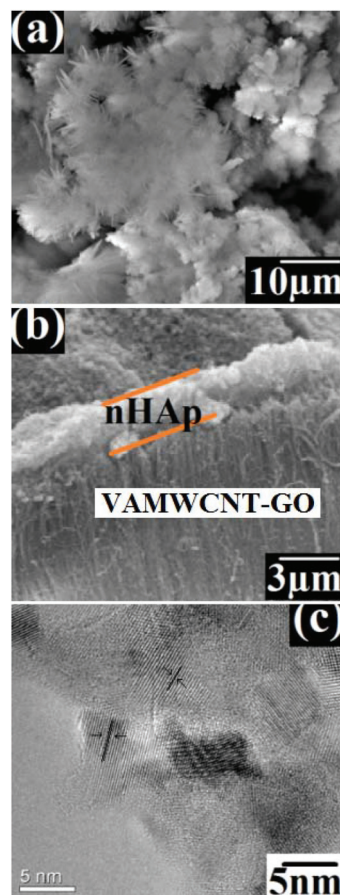
shows a top view of the polycrystalline nHAp coating, exhibiting different crystal shapes and orientations. One can notice many plate- and needle-like nHAp crystals surrounded by exfoliated nanotubes. More details of the length (1–3 μm), thickness (1–10 nm) and orientation of these crystals are shown in Fig. 6. The high level of porosity observed in all structures may be related either to the formation and entrapment of hydrogen bubbles during the electrodeposition process, or to the porous structure of the VAMWCNT–GO electrode. Fig. 5(b) shows that after 20 min deposition the thickness of the nHAp layer is about 3 μm, giving a growth rate of 0.15 μm min$^{-1}$. This growth rate is much higher than that of the apatite formed by soaking in the SBF, which could take as long as 3 weeks to obtain the same thickness.[17] Notice that a thin crystalline nHAp film was deposited on the top surface without affecting the alignment of the VAMWCNT–GO electrode. Furthermore, no apatite is apparent on the CNT walls. This indicates a heterogeneous electron transfer process, as proposed by Banks and Compton.[34] One may argue why HAp is being electrodeposited mainly on the CNT tips but not on their walls. The following hypotheses may be suggested to explain this phenomenon: (i) the electrolyte only spreads superficially and could not penetrate through the highly porous material. This
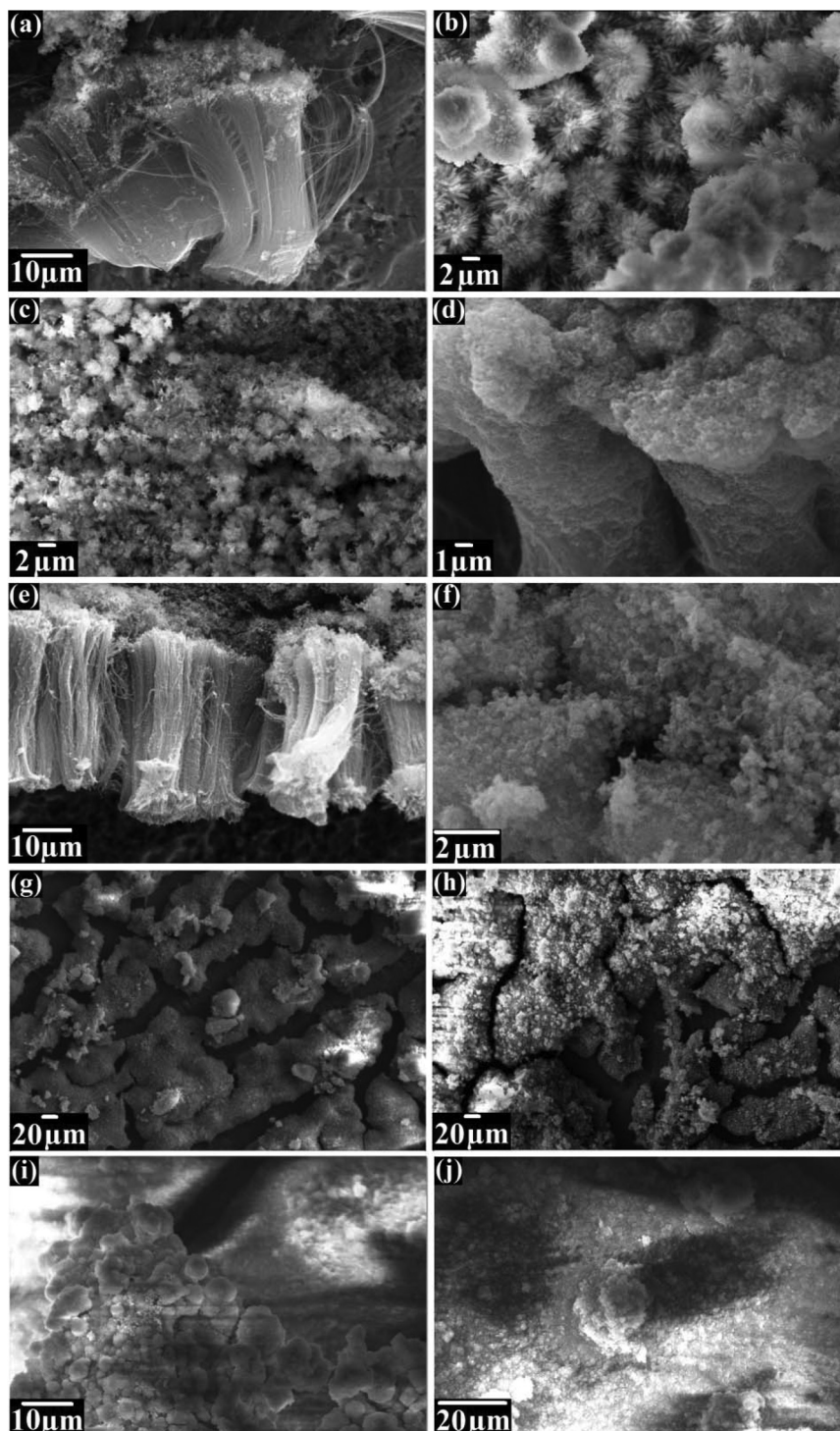
**Fig. 6** SEM micrographs of as electrodeposited nHAp−VAMWCNT−GO (a) before and after soaking in the SBF for (b) 0.5 h, (c) 1 h, (d) 2 h, (e) 4 h, (f) 6 h, (g) 12 h, (h) 1 day, (i) 2 days and (j) 7 days.

could be because the VAMWCNT tips are much more hydrophilic than their walls, or because atmospheric air remained trapped inside the porous material, or both. (ii) The edge plane of the graphene sheet is a few orders of magnitude more electroactive than that of the basal plane, showing also an accelerated charge-transfer rate. An electrochemical study of liquid penetration through highly densely packed aligned CNT electrodes is currently being undertaken in our group.

From the TEM micrographs in Fig. 5(c), the interplanar spacing of the nHAp crystals is measured as ~2.8 Å, which can

be related to the (112) and (002) planes, and is consistent with the crystallite size calculated based on XRD data. The small crystallite size may be due to a few factors, including the high density of carboxylate groups on the CNT surfaces, $H_2$ evolution during electrodeposition, and the abundant supply of coordination compounds available for complexation. Considering the latter, calcium and phosphate ions in the aqueous medium may have led to a very large number of nuclei during all stages of electrodeposition, favoring the emergence of new nucleation centers rather than the growth of the existing ones.

As we previously showed, the size of the nHAp crystals is related to these available nucleation sites.[1] The high number of nuclei facilitates homogeneous nucleation during electrodeposition, leading to precipitation and formation of small-size apatite on the VAMWCNT–GO electrodes.

### 3.3. Biomineralization analyses of nHAp–VAMWCNT–GO composites

The biomineralization process of the nHAp–VAMWCNT–GO composite after soaking in the SBF was confirmed by SEM analysis (Fig. 6) before and after soaking in the SBF for times ranging from 0 to 7 days, allowing the identification of the individual deposition steps. Fig. 6(a) shows a cross-section image of nHAp electrodeposited onto VAMWCNT–GO, illustrating that nHAp forms on the exfoliated CNT tips and that the length of the nanotubes is about ~40 μm. This sample was then placed into the SBF, and from Fig. 6(b) the biomineralization process is seen to begin with the clear formation of some isolated globular-like nHAp on nHAp–VAMWCNT–GO visible after 30 min of soaking. It is possible to see that needle-like nHAp starts to change its morphology to sphere-like shapes during the biomineralization. After 1 h soaking in the SBF, the isolated globular-like nHAp spreads over the surface, forming a continuous apatite layer over the entire surface (Fig. 6(c)). After 2 h, the apatite grows inside a dense pack of CNTs, spreading down and covering the CNT walls. The strong charging of the sample after 4 h soaking in the SBF during the SEM measurement indicates that the insulating apatite layer has covered the whole CNT surface from top to bottom. After 6 h the intrinsic stress in the thicker apatite film causes cracks at the surface of the composite. Large pores and small grains increase the dissolution rate, while nanosize pores may act as preferred sites for early nucleation and growth of apatite crystals.[35] This cracking increases up to 2 days, but then starts to be covered again as new apatite layers overgrow it. After 7 days (Fig. 6(j)) the composite is consolidated. Thus, soaking in the SBF is confirmed to be a simple and efficient method to cover the entire CNT matrix, including the tube walls.

Fig. 7 shows (a) the transient of the Ca/P ratio, (b) the Ca and P concentrations, (c) the oxygen content, and (d) the pH during soaking in the SBF. The "control" in this figure is as-electrodeposited nHAp, which had the stoichiometric composition of Ca/P = 1.67 (the chemical formula of HAp is $Ca_{10}(PO_4)_6(OH)_2$). Calcium is a common ion in SBFs and bioactive materials, and plays an important role in the process of dissolution/precipitation. Its release from the surface of the substrate to the adjacent electrolyte triggers the formation of the biologically active layer and stimulates bone growth.[36–38] The isoelectric point of HAp in water is at pH values ranging between 5 and 7,[39] and is lower than the pH of the SBF, which is ~7.4. Therefore, on immersion in the SBF, the HAp could exhibit a negative surface charge by exposing hydroxyl and phosphate groups.[40] This negative charge on the surface of the HAp is beneficial in the specific interaction with the positive calcium ions in the fluid, consequently forming a CHAp.[41] This electrodeposited nHAp was found to be an efficient inducer of nucleation of biological-like apatite in the SBF because it provides many hydroxyl terminals (negative charges) at the surface.

When the nHAp–VAMWCNT–GO is soaked in the SBF, the negatively charged surface preferentially adsorbs $Ca^{2+}$, thus promoting apatite nucleation on a calcified surface.[42] The adsorption of $Ca^{2+}$ ions from the solution may be associated with the initial formation of hydroxycarbonated apatite.[43,44] During the first hour of incubation, the Ca/P ratio increases due to Ca deposition, forming Ca-rich amorphous calcium phosphate, which promotes the positive charging of the surface.[45] Next, the Ca-rich CHAp starts to attract negative phosphate and carbonate ions from the SBF. After one hour, the concentration of Ca starts to decrease while that of P starts to increase (Fig. 7(b)).[46] Longer incubation in the SBF promotes the formation of a Ca-deficient CHAp layer, with a Ca/P ratio of about 1.55 after 48 h. A slight increase in the oxygen concentration at long incubation periods (Fig. 7(c)) is also observed. This can be explained in terms of $OH^-$ formation at long incubation periods, which is consistent with the FTIR results explained below (Fig. 8). The balance between the hydroxyl groups on the surface and in solution would affect the pH locally. Fig. 7(d) shows the pH variation of the SBF over time during soaking of nHAp–VAMWCNT–GO. In the first 30 minutes, the alkalizing effect can be attributed to both the release of hydroxyl ions from the surface of nHAp–VAMWCNT–GO, which react with $H^+$ in the electrolyte and the dissociation of $CaCl_2 \cdot 2H_2O$, which release $Ca^{2+}$ and $Cl^-$ ions into the medium. Also, the dissociation of $K_2HPO_4$ in water releases an extremely strong base $OH^-$ to the medium. Under these conditions, the $Ca^{2+}$ cations attract both the $H_2PO_4^-$ anions and $OH^-$ anions, forming HAp ($Ca_5(PO_4)_3(OH)$) nuclei. Removal of hydroxyls during HAp production together with $CO_3^{2-}$ production increases the acidity of the medium as the reactions proceed. After few days of soaking in the SBF medium, Ca-poor CHAp formation eventually becomes favorable and the pH becomes more alkaline, reaching ~7.25 due to many salt ions (e.g. $Mg^{2+}$ and $Cl^-$) remaining in solution.

Fig. 8 shows the ATR-FTIR spectra of nHAp–VAMWCNT–GO before and after soaking in the SBF for periods up to 7 days. The absorption bands were found to fit those reported elsewhere for nHAp.[47,48] In these spectra, the multiplets located around 1000 cm$^{-1}$ are attributed to phosphate ($PO_4^{3-}$) modes. The band at 1090 cm$^{-1}$ and the doublet at ~1024 cm$^{-1}$ are assigned to components of the triply degenerate $\nu_3$ antisymmetric PO stretching mode. The 961 cm$^{-1}$ band is assigned to
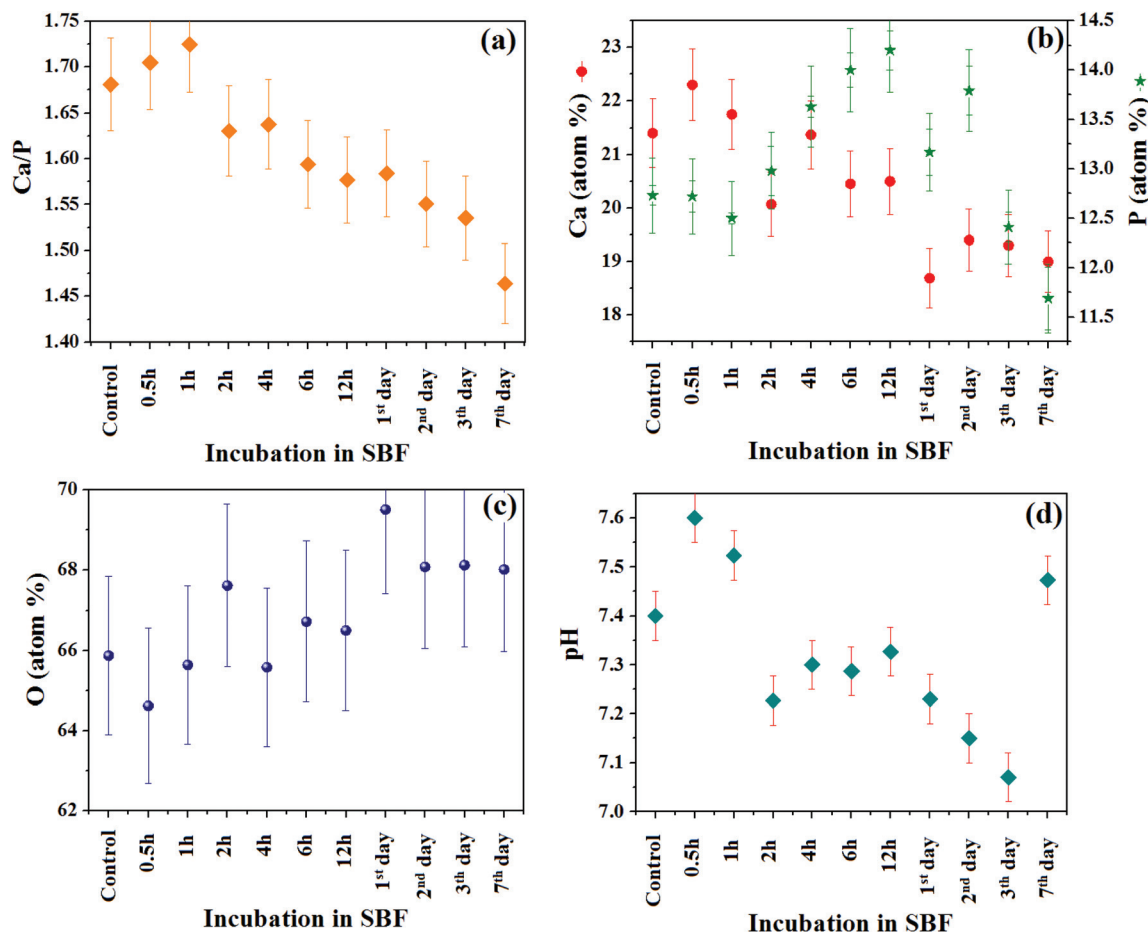
**Fig. 7** EDS semiquantitative chemical analyses of the Ca/P atomic ratio (a) concentrations of Ca, P (b) and O (c) in nHAp–VAMWCNT–GO soaked in the SBF between 30 min and 7 days. Each point is the average of three samplings in different regions on the surface. (d) pH transient during incubation in the SBF.
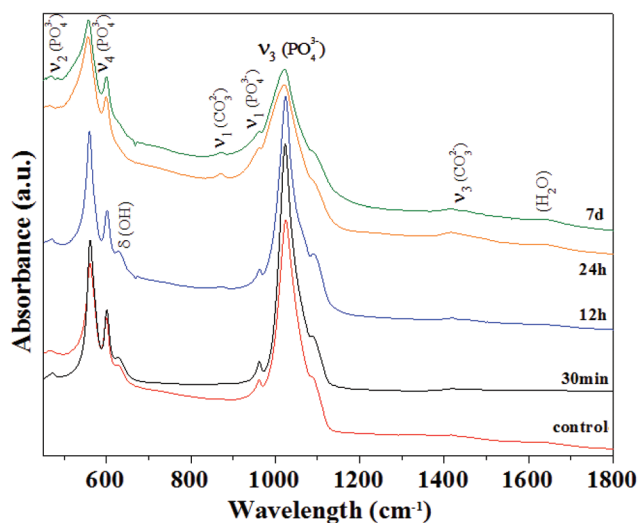


**Fig. 8** ATR-FTIR spectra of biomimetic apatite coating on the nHAp–VAMWCNT–GO substrate as a function of time being soaked in the SBF.

$\nu_1$, the non-degenerate PO symmetric-stretching mode. The bands at ∼600 and 562 cm$^{-1}$ are assigned to components of the triply degenerate $\nu_4$ OPO bending mode, whereas the band at 466 cm$^{-1}$ is assigned to components of the doubly degenerate $\nu_2$ OPO bending mode.[47]

Carbonate bands are detected at 879 and 1420 cm$^{-1}$.[49] Both the intensity and the area of these bands increased with the time of immersion in the SBF, thus showing that carbonate formation is favourable. The carbonate ($CO_3^{2-}$) originates from the $NaHCO_3$ in the medium, which decomposes to NaH + $CO_3^{2-}$, increasing the pH. The presence of $CO_3^{2-}$ functional groups suggests that carbonate ions are incorporated into the biomimetic apatite and form CHAp.[50]

Furthermore, a band at 635 cm$^{-1}$, which is attributed to ($\delta$) OH$^-$ groups,[48] reduces during the biomimetic apatite coating formation, which is consistent with carbonate formation. Crystallization of the amorphous CHAp film takes place by incorporation of OH$^-$ and/or carbonate anions from solution to form a mixed hydroxyl-carbonate layer. The observed bands at 3400 (not shown) and 1640 cm$^{-1}$ in all spectra correspond to water adsorption during the biomimetic apatite formation.[33]
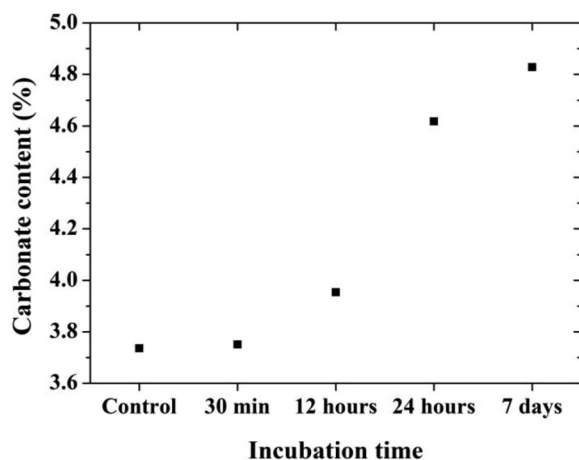
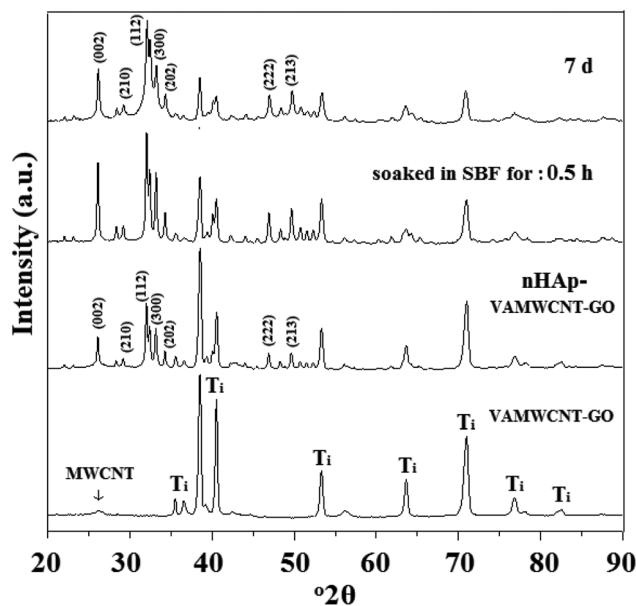Fig. 9 Total carbonate content in nHAp : VAMWCNT–GO before and after soaking in the SBF for up to 7 days.



Fig. 10 X-ray diffractograms of biomimetic apatite coating on the nHAp–VAMWCNT–GO composite demonstrating the effect of soaking time in the SBF. Carbonated-apatite is indexed with respect to JCPDS card 00-004-0697.

The intensity ratio between the carbonate band (1420 cm$^{-1}$) and the phosphate band (598 cm$^{-1}$), $I_C/I_P$, was used to estimate the carbonate ion content, (% $y$), in the nHAp lattice for the case of B-type substitution, according to eqn (1).[35]

$$\%y_{CO_3} = 10.134\left(\frac{I_C}{I_P}\right) + 0.2134 \qquad (1)$$

Fig. 9 shows the carbonate content of nHAp–VAMWCNT–GO before and after soaking in the SBF. As-grown nHAp–VAMWCNT–GO contains ~3.8% carbonate. However, this value increased to ~4.8% after 7 days soaking.

The formation of the Ca-rich layer is assumed to take place by consecutive accumulation of the calcium ions, which makes the Ca-rich layer acquire and increase positive charge. The CHAp on the HAp therefore interacts specifically with the negative phosphate ions in the fluid to form a Ca-poor layer. This type of Ca-poor apatite has been observed as a precursor, which eventually crystallizes into bonelike apatite on various bioactive ceramics.[51–54] The solubility of hydroxyapatite is lower than other calcium phosphate phases in water, and therefore thermodynamically the Ca-poor CHAP could be stabilized by transforming into a crystal phase of apatite in the SBF.[36] Once formed in the SBF that is supersaturated with respect to the apatite, the apatite grows spontaneously, consuming the calcium and phosphate ions, incorporating minor ions such as sodium, magnesium and carbonate, and thereby developing bone-like compositional and structural characteristics. During the biomineralization in the SBF solution, calcium carbonate and amorphous calcium phosphate form on the surface due to the migration of $Ca^{2+}$, $CaO_3^{2-}$ and $PO_4^{2-}$ by ion transfer channels, and all these events lead to the formation of new apatite crystals that are similar to those in bone tissue.[55]

Fig. 10 shows the XRD spectra of nHAp–VAMWCNT–GO before and after soaking in the SBF for up to 7 days. The VAMWCNT–GO shows characteristic C (sp$^2$ hybridization) and

Ti (substrate) crystallographic structures. We used three Joint Committee on Powder Diffraction Standards (JCPDS) cards to index all reflections: 04-0697 for HAp, 024-0033 for CNT and 044-0951 for Ti. Table 2 shows the crystallite size of the two most intense planes, showing that both peaks slightly shift to higher angles after soaking in the SBF solution. In addition, as a result of soaking, a CHAp phase forms. This phase is somewhat more brittle and weaker.[56] The peak centred at $2\theta \sim 32°$ is typical of the hexagonal structure (p63 m) and is assigned to the (002) plane of HAp. The peak centered at $2\theta \sim 26.1°$ related to the (112) plane is the strongest reflection in the XRD pattern. A new phase was detected by observing the shift in the characteristic HAp peaks toward higher angles. The shift of peak positions and the change in crystallite size are consistent with alternating formation of Ca-rich and Ca-deficient apatites during incubation in the SBF. Peak positions are related to the interplanar spacing, $d$, for a given ($hkl$) reflection given by the hexagonal unit cell dimensions calculated using Bragg's Law, $\lambda = 2d_{hkl}\sin\theta_{hkl}$, where $(1/d^2) = (4/3)\{(h^2 + hk + k^2)/a^2\} + (l^2/c^2)$, where $a = 9.423$ Å and $c = 6.883$ Å.

The pattern shows all the Bragg peaks corresponding characteristically to CHAp, showing its structural integrity.[57] Though it is noticed that there is no major difference between CHAp and HAp, still there is a *slight* change observed in their unit cell parameters.

The calculated interplanar spacing presented in Table 2 is consistent with the TEM data. Also, the shift and decrease in crystallinity of HAp clearly indicate the occurrence of bonding between HAp particles and composites. Most of the HAp peaks show a clear shift after composite formation. Thus, a compari-

**Table 2** The change in interplanar spacing and crystallite size for two reflections of carbonated hydroxyapatite as a function of soaking time in the SBF

| Sample | $(2\theta)$ Peak (112) | $d$ (Å) | Crystallite (Å) | $(2\theta)$ Peak (002) | Crystallite (Å) | $d$ (Å) |
|--------|------------------------|---------|------------------|------------------------|------------------|---------|
| 0 | 31.96° | 2.80 | 617 | 26.04° | 697 | 3.42 |
| 30 min | 31.99° | 2.80 | 449 | 26.05° | 540 | 3.42 |
| 60 min | 31.99° | 2.80 | 547 | 26.05° | 540 | 3.42 |
| 2 h | 31.97° | 2.80 | 547 | 26.1° | 488 | 3.41 |
| 4 h | 32.08° | 2.79 | 617 | 26.1° | 540 | 3.41 |
| 6 h | 32.02° | 2.79 | 706 | 26.1° | 609 | 3.41 |
| 12 h | 32.05° | 2.79 | 617 | 26.1° | 697 | 3.42 |
| 24 h | 31.99° | 2.80 | 826 | 26.1° | 697 | 3.41 |
| 48 h | 32.00° | 2.80 | 411 | 26.1° | 443 | 3.41 |
| 72 h | 32.00° | 2.80 | 617 | 26.1° | 697 | 3.41 |
| 7 d | 32.09° | 2.79 | 547 | 26.1° | 961 | 3.41 |

son of the FTIR analysis has indicated that there is a chemical bonding at the interface between the nanoparticles and the consolidated composite.[58]

The results of XRD are consistent with the SEM, EDS and FTIR data, and show that apatite, indeed, formed on the surface of the VAMWCNT–GO composite. This coated composite has a potential use in biological applications. Moreover, these data allow us to hypothesize the mechanism of nHAp formation on VAMWCNT–GO, as discussed in section 3.4.

### 3.4. Proposed mechanism of nHAp–VAMWCNT–GO composite formation

Fig. 11 presents schematically the steps of nHAp–VAMWCNT–GO preparation and biomineralization, as we envision them. The first two images on the left show as-grown VAMWCNT and VAMWCNT–GO.
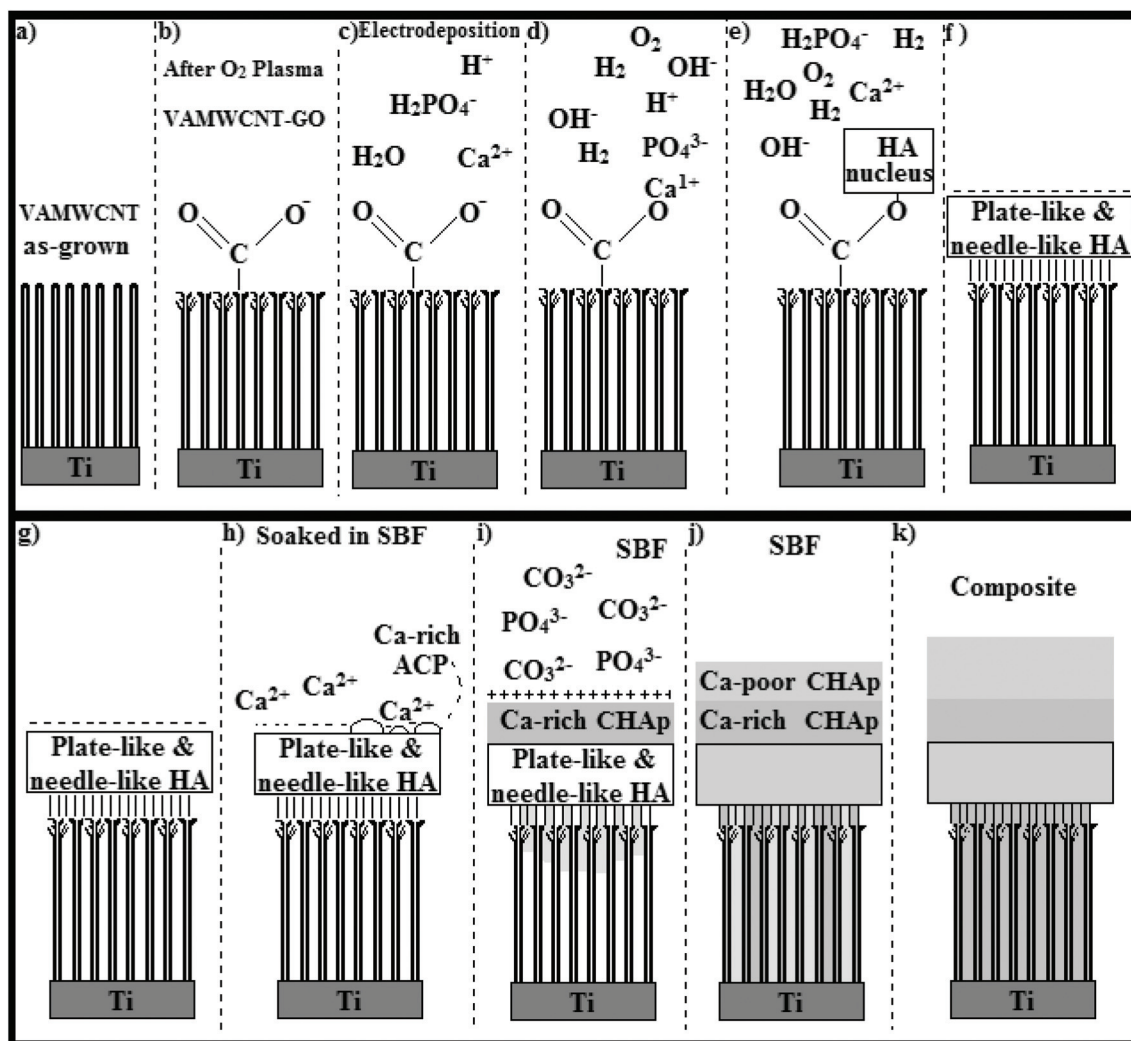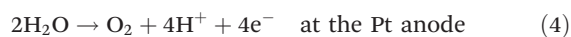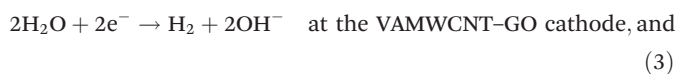


**Fig. 11** Proposed *in vitro* biomineralization process of precipitation of CHAp on nHAp–VAMWCNT–GO composites.

**3.4.1 Mechanism of nHAp formation on VAMWCNT–GO by electrodeposition.** The electrodeposition of HAp is taking place in parallel with extensive hydrogen evolution, which reduces precursor compounds from both the solution and the electrode surface. The initial pH of the solution was 5.8, which reduced to 5.6 after 20 min of deposition due to the formation of acidic species. Once hydroxyl ions are generated on the VAMWCNT–GO electrode, an acid–base reaction takes place, forming $H_2PO_4^-$ and $HPO_4^{2-}$, which are major species in the precipitation of calcium phosphates on electrode surfaces.

Mixing $(NH_4)H_2PO_4$ and $Ca(NO_3)_2$ produces $NH_4NO_3$, see eqn (2). This compound is slightly acidic and very soluble, which does not contribute to precipitation during deposition of nHAp:

$$2(NH_4)H_2PO_4 + Ca(NO_3)_2 \rightarrow 2NH_4NO_3 + Ca^{2+} + 2H_2PO_4^- \tag{2}$$
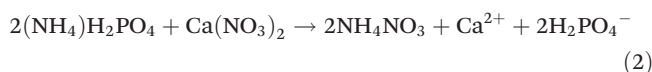
The precipitation of HAp requires $OH^-$ ions, which originate from water splitting:

$$2H_2O + 2e^- \rightarrow H_2 + 2OH^- \quad \text{at the VAMWCNT–GO cathode, and} \tag{3}$$

$$2H_2O \rightarrow O_2 + 4H^+ + 4e^- \quad \text{at the Pt anode} \tag{4}$$

Some of the $OH^-$ produced at the cathode (4) is consumed during electrodeposition of HAp as follows:

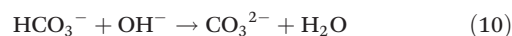$$10Ca^{2+} + 6H_2PO_4^- + 14OH^- \rightarrow Ca_{10}(PO_4)_6(OH)_2 + 12H_2O \tag{5}$$
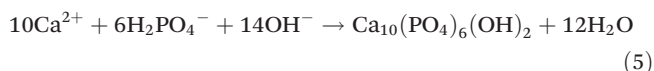
Combining eqn (3) through (5), we have HAp on VAMWCNT–GO, with $H_2$ (cathode) and $O_2$ (anode) evolution and decrease of pH of the solution due to the formation of $H^+$.

During electrodeposition, the combination of $Ca^{2+}$, $H_2PO_4^-$ and $OH^-$ forms HAp nuclei (Fig. 11c–e), which will accelerate the deposition of the coalesced film of plate-like and needle-like apatites (Fig. 11f). This apatite film, when soaked in the SBF, shows bioactivity by forming a globular-like CHAp.

**3.4.2 Mechanism of CHAp formation on the nHAp–VAMWCNT–GO bio-scaffold by SBF immersion.** The globular-like CHAp phase forms as a result of electrostatic forces between positive calcium ions eqn(6) in the SBF and the negatively charged surface of electrodeposited HAp. The electrodeposited film exposes to the solution negative hydroxyl and phosphate components in its crystal structure due to its iso-electric point of about 5–7, which is lower than the pH of the SBF (~7.4 and fairly stable for long time). This negatively charged surface attracts ions from the dissociation presented in eqn (6) through (8), which balance for more alkaline pH. Under these conditions, the $Ca^{2+}$ cations bond to nHAp–VAMWCNT–GO and attract both the $H_2PO_4^-$ anions and $OH^-$ anions from the medium, forming HAp ($Ca_5(PO_4)_3(OH)$) nuclei (Fig. 11h, i). Removal of hydroxyls during HAp production together with $CO_3^{2-}$ production increases the acidity of the medium as the reactions proceed. The formation of Ca-rich CHAp progressively changes the surface charge, inducing

$PO_4^{3-}$ and $CO_3^{2-}$ competitive adsorption. The consequence is the formation of Ca-poor CHAp, which has been documented to take place in the process of apatite formation on various bioactive ceramics (Fig. 11j, k).

$$CaCl_2 \rightarrow Ca^{2+} + 2Cl^- \tag{6}$$

$$K_2HPO_4 \rightarrow 2K^+ + HPO_4^{2-} \tag{7}$$

$$HPO_4^{2-} + H_2O \rightarrow H_2PO_4^- + OH^- \tag{8}$$

$$NaHCO_3 \rightarrow Na^+ + HCO_3^- \tag{9}$$

$$HCO_3^- + OH^- \rightarrow CO_3^{2-} + H_2O \tag{10}$$

# 4. Conclusions

This paper describes a novel method of forming a nHAp–VAMWCNT–GO composite. The first stage is the exfoliation of vertically aligned multi-walled carbon nanotubes (VAMWCNTs) by oxygen plasma etching (OPE), which attaches oxygen-containing groups onto the tips of the CNTs and renders them hydrophilic. Following this step, plate-like and needle-like nano-hydroxyapatite (nHAp) films can be electrodeposited, thus forming a nHAp–VAMWCNT–GO composite. This composite is bioactive in the SBF, forming either calcium-rich or calcium-poor layers, depending on the incubation period, which consolidates into a thick, dense composite after approximately one week. A method for deposition of apatite is described. The nHAp–VAMWCNT–GO composite is characterized by a bioactive surface, which could accelerate bone formation and implant fixation, while being a cheap material. Further investigation is required to verify cytotoxicity and *in vivo* bioactivity. This is already underway in our group, and its results will be in the subject of a future publication.

# Acknowledgements

# References

1 H. Zanin, E. Saito, F. R. Marciano, H. J. Ceragioli, A. E. Campos Granato, M. Porcionatto and A. O. Lobo, Fast preparation of nano-hydroxyapatite/superhydrophilic reduced graphene oxide composites for bioactive applications, *J. Mater. Chem. B*, 2013, **1**, 4947–4955.

2 N. Eliaz and M. Eliyahu, Electrochemical processes of nucleation and growth of hydroxyapatite on titanium

supported by real-time electrochemical atomic force microscopy, *J. Biomed. Mater. Res., Part A*, 2007, **80A**, 621–634.

3  H. Wang, N. Eliaz and L. W. Hobbs, The nanostructure of an electrochemically deposited hydroxyapatite coating, *Mater. Lett.*, 2011, **65**, 2455–2457.

4  U. S. Shin, I.-K. Yoon, G.-S. Lee, W.-C. Jang, J. C. Knowles and H.-W. Kim, Carbon nanotubes in nanocomposites and hybrids with hydroxyapatite for bone replacements, *J. Tissue Eng.*, 2011, **2011**, 674287–674287.

5  A. A. White, S. M. Best and I. A. Kinloch, Hydroxyapatite-carbon nanotube composites for biomedical applications: A review, *Int. J. Appl. Ceram. Technol.*, 2007, **4**, 1–13.

6  L. Zhang, W. Liu, C. Yue, T. Zhang, P. Li, Z. Xing and Y. Chen, A tough graphene nanosheet/hydroxyapatite composite with improved in vitro biocompatibility, *Carbon*, 2013, **61**, 105–115.

7  M. Mehrali, E. Moghaddam, S. F. S. Shirazi, S. Baradaran, M. Mehrali, S. T. Latibari, H. S. C. Metselaar, N. A. Kadri, K. Zandi and N. A. Abu Osman, Synthesis, Mechanical Properties, and in Vitro Biocompatibility with Osteoblasts of Calcium Silicate-Reduced Graphene Oxide Composites, *Acs Appl. Mater. Interfaces*, 2014, **6**, 3947–3962.

8  D. Lahiri, A. P. Benaduce, L. Kos and A. Agarwal, Quantification of carbon nanotube induced adhesion of osteoblast on hydroxyapatite using nano-scratch technique, *Nanotechnology*, 2011, 22.

9  K. Balani, R. Anderson, T. Laha, M. Andara, J. Tercero, E. Crumpler and A. Agarwal, Plasma-sprayed carbon nanotube reinforced hydroxyapatite coatings and their interaction with human osteoblasts in vitro, *Biomaterials*, 2007, **28**, 618–624.

10  P. C. Rath, B. P. Singh, L. Besra and S. Bhattacharjee, Multiwalled Carbon Nanotubes Reinforced Hydroxyapatite-Chitosan Composite Coating on Ti Metal: Corrosion and Mechanical Properties, *J. Am. Ceram. Soc.*, 2012, **95**, 2725–2731.

11  O. Im, J. Li, M. Wang, L. G. Zhang and M. Keidar, Biomimetic three-dimensional nanocrystalline hydroxyapatite and magnetically synthesized single-walled carbon nanotube chitosan nanocomposite for bone regeneration, *Int. J. Nanomed.*, 2012, **7**, 2087–2099.

12  D.-Y. Kim, Y.-H. Han, J. H. Lee, I.-K. Kang, B.-K. Jang and S. Kim, Characterization of multiwalled carbon nanotube-reinforced hydroxyapatite composites consolidated by spark plasma sintering, *BioMed Res. Int.*, 2014, **2014**, 768254–768254.

13  A. O. Lobo, M. A. F. Corat, S. C. Ramos, J. T. Matsushima, A. E. C. Granato, C. Pacheco-Soares and E. J. Corat, Fast Preparation of Hydroxyapatite/Superhydrophilic Vertically Aligned Multiwalled Carbon Nanotube Composites for Bioactive Application, *Langmuir*, 2010, **26**, 18308–18314.

14  M. M. Zogbi Jr., E. Saito, H. Zanin, F. R. Marciano and A. O. Lobo, Hydrothermal-electrochemical synthesis of nano-hydroxyapatite crystals on superhydrophilic vertically aligned carbon nanotubes, *Mater. Lett.*, 2014, **132**, 70–74.

15  M. Kawashita, M. Nakao, M. Minoda, H. M. Kim, T. Beppu, T. Miyamoto, T. Kokubo and T. Nakamura, Apatite-forming ability of carboxyl group-containing polymer gels in a simulated body fluid, *Biomaterials*, 2003, **24**, 2477–2484.

16  M. Lee, S. H. Ku, J. Ryu and C. B. Park, Mussel-inspired functionalization of carbon nanotubes for hydroxyapatite mineralization, *J. Mater. Chem.*, 2010, **20**, 8848–8853.

17  T. C. O. Marsi, T. G. Santos, C. Pacheco-Soares, E. J. Corat, F. R. Marciano and A. O. Lobo, Biomineralization of Superhydrophilic Vertically Aligned Carbon Nanotubes, *Langmuir*, 2012, **28**, 4413–4424.

18  F. Barrere, M. M. E. Snel, C. A. van Blitterswijk, K. de Groot and P. Layrolle, Nano-scale study of the nucleation and growth of calcium phosphate coating on titanium implants, *Biomaterials*, 2004, **25**, 2901–2910.

19  H. Zanin, P. W. May, D. J. Fermin, D. Plana, S. M. C. Vieira, W. I. Milne and E. J. Corat, Porous Boron-Doped Diamond/Carbon Nanotube Electrodes, *ACS Appl. Mater. Interfaces*, 2014, **6**, 990–995.

20  A. O. Lobo, S. C. Ramos, E. F. Antunes, F. R. Marciano, V. J. Trava-Airoldi and E. J. Corat, Fast functionalization of vertically aligned multiwalled carbon nanotubes using oxygen plasma, *Mater. Lett.*, 2012, **70**, 89–93.

21  H. Zanin, E. Saito, H. J. Ceragioli, V. Baranauskas and E. J. Corat, Reduced graphene oxide and vertically aligned carbon nanotubes superhydrophilic films for supercapacitors devices, *Mater. Res. Bull.*, 2014, **49**, 487–493.

22  K. Li, G. Eres, J. Howe, Y.-J. Chuang, X. Li, Z. Gu, L. Zhang, S. Xie and Z. Pan, Self-Assembly of Graphene on Carbon Nanotube Surfaces, *Sci. Rep.*, 2013, 3.

23  J. Zhou, H. Song, B. Fu, B. Wu and X. Chen, Synthesis and high-rate capability of quadrangular carbon nanotubes with one open end as anode materials for lithium-ion batteries, *J. Mater. Chem.*, 2010, **20**, 2794–2800.

24  E. F. Antunes, A. O. Lobo, E. J. Corat, V. J. Trava-Airoldi, A. A. Martin and C. Verissimo, Comparative study of first- and second-order Raman spectra of MWCNT at visible and infrared laser excitation, *Carbon*, 2006, **44**, 2202–2211.

25  H. Zanin, A. Margraf-Ferreira, N. S. da Silva, F. R. Marciano, E. J. Corat and A. O. Lobo, Graphene and carbon nanotube composite enabling a new prospective treatment for trichomoniasis disease, *Mater. Sci. Eng., C*, 2014, **41**, 65–69.

26  Y. Liu, R. Deng, Z. Wang and H. Liu, Carboxyl-functionalized graphene oxide-polyaniline composite as a promising supercapacitor material, *J. Mater. Chem.*, 2012, **22**, 13619–13624.

27  T. A. Silva, H. Zanin, F. C. Vicentini, E. J. Corat and O. Fatibello-Filho, Differential pulse adsorptive stripping voltammetric determination of nanomolar levels of atorvastatin calcium in pharmaceutical and biological samples using a vertically aligned carbon nanotube/graphene oxide electrode, *Analyst*, 2014, **139**, 2832–2841.

28  V. Datsyuk, M. Kalyva, K. Papagelis, J. Parthenios, D. Tasis, A. Siokou, I. Kallitsis and C. Galiotis, Chemical oxidation

of multiwalled carbon nanotubes, *Carbon*, 2008, **46**, 833–840.

29  S. Kundu, Y. Wang, W. Xia and M. Muhler, Thermal Stability and Reducibility of Oxygen-Containing Functional Groups on Multiwalled Carbon Nanotube Surfaces: A Quantitative High-Resolution XPS and TPD/TPR Study, *J. Phys. Chem. C*, 2008, **112**, 16869–16878.

30  B. P. Payne, M. C. Biesinger and N. S. McIntyre, X-ray photoelectron spectroscopy studies of reactions on chromium metal and chromium oxide surfaces, *J. Electron Spectrosc. Relat. Phenom.*, 2011, **184**, 29–37.

31  L. M. Hollanda, A. O. Lobo, M. Lancellotti, E. Berni, E. J. Corat and H. Zanin, Graphene and carbon nanotube nanocomposite for gene transfection, *Mater. Sci. Eng., C*, 2014, **39**, 288–298.

32  T. A. Silva, H. Zanin, E. Saito, R. A. Medeiros, F. C. Vicentini, E. J. Corat and O. Fatibello-Filho, Electrochemical behaviour of vertically aligned carbon nanotubes and graphene oxide nanocomposite as electrode material, *Electrochim. Acta*, 2014, **119**, 114–119.

33  N. Eliaz and T. M. Sridhar, Electrocrystallization of Hydroxyapatite and Its Dependence on Solution Conditions, *Cryst. Growth Des.*, 2008, **8**, 3965–3977.

34  C. E. Banks and R. G. Compton, Edge plane pyrolytic graphite electrodes in electroanalysis: An overview, *Anal. Sci.*, 2005, **21**, 1263–1268.

35  R. Z. LeGeros, Calcium phosphates in oral biology and medicine, *Monogr. Oral Sci.*, 1991, **15**, 1–201.

36  M. Piedad Ramirez-Fernandez, J. Luis Calvo-Guirado, J. Eduardo Mate-Sanchez del Val, R. Arcesio Delgado-Ruiz, B. Negri and C. Barona-Dorado, Ultrastructural study by backscattered electron imaging and elemental microanalysis of bone-to-biomaterial interface and mineral degradation of porcine xenografts used in maxillary sinus floor elevation, *Clin. Oral Implants Res.*, 2013, **24**, 523–530.

37  D. Lakstein, W. Kopelovitch, Z. Barkay, M. Bahaa, D. Hendel and N. Eliaz, Enhanced osseointegration of grit-blasted, NaOH-treated and electrochemically hydroxyapatite-coated Ti-6Al-4 V implants in rabbits, *Acta Biomater.*, 2009, **5**, 2258–2269.

38  N. Eliaz, S. Shmueli, I. Shur, D. Benayahu, D. Aronov and G. Rosenman, The effect of surface treatment on the surface texture and contact angle of electrochemically deposited hydroxyapatite coating and on its interaction with bone-forming cells, *Acta Biomater.*, 2009, **5**, 3178–3191.

39  P. Somasundaran and B. Markovic, Interfacial properties of calcium phosphates. in: *Calcium Phosphate in Biological and Industrial Systems*, ed. Z. Amjad, Trans. Tech. Pub., Switzerland, 1998, pp. 85–101.

40  J. C. Elliot, *Structure and Chemistry of the Apatites and other Calcium Orthophosphates*, Elsevier Sci., Amsterdam, 1994.

41  H. M. Kim, T. Himeno, T. Kokubo and T. Nakamura, Process and kinetics of bonelike apatite formation on sintered hydroxyapatite in a simulated body fluid, *Biomaterials*, 2005, **26**, 4366–4373.

42  H. M. Kim, T. Himeno, T. Kokubo and T. Nakamura, Process and kinetics of bonelike apatite formation on sintered hydroxyapatite in a simulated body fluid, *Biomaterials*, 2005, **26**, 4366–4373.

43  M. U. Hashmi, S. A. Shah, S. Alam and A. Shamim, Dissolution behavior of bioactive glass ceramics with different cao/mgo ratios, *Ceram.-Silik.*, 2010, **54**, 8–13.

44  A. O. Lobo, H. Zanin, I. A. W. B. Siqueira, N. C. S. Leite, F. R. Marciano and E. J. Corat, Effect of ultrasound irradiation on the production of nHAp/MWCNT nanocomposites, *Mater. Sci. Eng., C*, 2013, **33**, 4305–4312.

45  G. Y. Liu, J. Hu, Z. K. Ding and C. Wang, Bioactive calcium phosphate coating formed on micro-arc oxidized magnesium by chemical deposition, *Appl. Surf. Sci.*, 2011, **257**, 2051–2057.

46  A. Hoppe, J. Will, R. Detsch, A. R. Boccaccini and P. Greil, Formation and in vitro biocompatibility of biomimetic hydroxyapatite coatings on chemically treated carbon substrates, *J. Biomed. Mater. Res., Part A*, 2014, **102**, 193–203.

47  B. O. Fowler, Infrared studies of apatites .1. Vibrational assignments for calcium, strontium, and barium hydroxyapatites utilizing isotopic-substitution, *Inorg. Chem.*, 1974, **13**, 194–207.

48  A. Paz, D. Guadarrama, M. Lopez, J. E. Gonzalez, N. Brizuela and J. Aragon, A comparative study of hydroxyapatite nanoparticles synthesized by different routes, *Quim. Nova*, 2012, **35**, 1724–1727.

49  D. R. Taylor, R. S. Crowther, J. C. Cozart, P. Sharrock, J. G. Wu and R. D. Soloway, Calcium-carbonate in cholesterol gallstones - polymorphism, distribution, and hypotheses about pathogenesis, *Hepatology*, 1995, **22**, 488–496.

50  Y. F. Chou, W. A. Chiou, Y. H. Xu, J. C. Y. Dunn and B. M. Wu, The effect of pH on the structural evolution of accelerated biomimetic apatite, *Biomaterials*, 2004, **25**, 5323–5331.

51  L. L. Hench, Bioceramics - from concept to clinic, *J. Am. Ceram. Soc.*, 1991, **74**, 1487–1510.

52  M. Neo, T. Nakamura, C. Ohtsuki, T. Kokubo and T. Yamamuro, Apatite formation on 3 kinds of bioactive material at an early-stage *in vivo* - a comparative-study by transmission electron-microscopy, *J. Biomed. Mater. Res.*, 1993, **27**, 999–1006.

53  M. R. Filgueiras, G. Latorre and L. L. Hench, Solution effects on the surface-reactions of a bioactive glass, *J. Biomed. Mater. Res.*, 1993, **27**, 445–453.

54  C. Ohtsuki, T. Kokubo and T. Yamamuro, Mechanism of apatite formation on cao-sio2-p2o5 glasses in a simulated body-fluid, *J. Non-Cryst. Solids*, 1992, **143**, 84–92.

55  Y. Guo, Y. Zhou, D. Jia and H. Tang, Fabrication and characterization of hydroxycarbonate apatite with mesoporous structure, *Microporous Mesoporous Mater.*, 2009, **118**, 480–488.

56  G. A. Stanciu, I. Sandulescu, B. Savu, S. G. Stanciu, K. M. Paraskevopoulos, X. Chatzistavrou, E. Kontonasaki and P. Koidis, Investigation of the hydroxyapatite growth

on bioactive glass surface, *J. Biomed. Pharm. Eng.*, 2007, **1**, 34–39.

57  R. Murugan, K. P. Rao and T. S. S. Kumar, Microwave synthesis of bioresorbable carbonated hydroxyapatite using goniopora, *Bioceramics*, 2002, **15**, 51–54.

58  N. Pramanik, D. Mishra, I. Banerjee, T. K. Maiti, P. Bhargava and P. Pramanik, Chemical synthesis, characterization, and biocompatibility study of hydroxyapatite/ chitosan phosphate nanocomposite for bone tissue engineering applications, *Int. J. Biomater.*, 2009, 512417–512417.